Rostro-caudal Architecture of the Frontal Lobes in Humans

Michel Thiebaut de Schotten, Marika Urbanski, Benedicte Batrancourt, Richard Levy, Bruno Dubois, Leonardo Cerliani, Emmanuelle Volle

To cite this version:

Michel Thiebaut de Schotten, Marika Urbanski, Benedicte Batrancourt, Richard Levy, Bruno Dubois, et al.. Rostro-caudal Architecture of the Frontal Lobes in Humans. Cerebral Cortex, 2016, 27 (8), pp.4033-4047. 10.1093/cercor/bhw215 . hal-04412827

Cerebral Cortex, August 2017;27: 4033–4047

doi: 10.1093/cercor/bhw215
Advance Access Publication Date: 26 July 2016
Original Article

ORIGINAL ARTICLE

Rostro-caudal Architecture of the Frontal Lobes in Humans

Michel Thiebaut de Schotten[1,2,3], Marika Urbanski[1,2,4], Benedicte Batrancourt[1,2], Richard Levy[2], Bruno Dubois[2], Leonardo Cerliani[1,2], and Emmanuelle Volle[1,2,3]

[1]Brain Connectivity and Behaviour Group, Brain and Spine Institute, Paris, France, [2]Frontlab, Institut du Cerveau et de la Moelle épinière (ICM), UPMC UMRS 1127, Inserm U 1127, CNRS UMR 7225, Paris, France, [3]Centre de Neuroimagerie de Recherche CENIR, Groupe Hospitalier Pitié-Salpêtrière, Paris, France, and [4]Service de Médecine et de Réadaptation, Hôpitaux de Saint-Maurice, Saint-Maurice, France

Address correspondence to Dr Michel Thiebaut de Schotten. Email: michel.thiebaut@gmail.com

Abstract

The nature of the inputs and outputs of a brain region defines its functional specialization. The frontal portion of the brain is essential for goal-directed behaviors, however, the biological basis for its functional organization is unknown. Here, exploring structural connectomic properties, we delineated 12 frontal areas, defined by the pattern of their white matter connections. This result was highly reproducible across neuroimaging centers, acquisition parameters, and participants. These areas corresponded to regions functionally engaged in specific tasks, organized along a rostro-caudal axis from the most complex high-order association areas to the simplest idiotopic areas. The rostro-caudal axis along which the 12 regions were organized also reflected a gradient of cortical thickness, myelination, and cell body density. Importantly, across the identified regions, this gradient of microstructural features was strongly associated with the varying degree of information processing complexity. These new anatomical signatures shed light onto the structural organization of the frontal lobes and could help strengthen the prediction or diagnosis of neurodevelopmental and neurodegenerative disorders.

Key words: frontal lobes, anatomy, cytoarchitecture, tractography, myeloarchitecture

Introduction

Knowledge of neuroanatomy is paramount to the study of brain function, anatomy, and physiology, all being integral components of the same science (Blits 1999). Anatomy and function are tantamount, and in evolutionary terms, function may probably have influenced anatomy (Aristotle 350BC reprinted in 2004). Functional models of the frontal lobes suggest a rostro-caudal organization that is essential for goal-directed behavior, in which low processing-level posterior regions receive signals from higher processing-level anterior regions (Mesulam 2000; Badre and D'Esposito 2007; Badre 2008; Badre and D'Esposito 2009; Christoff et al. 2009). The processing-level of these regions may depend upon the level of cognitive control with regard to relational complexity, as demonstrated in functional magnetic resonance imaging (*f*MRI) (Christoff et al. 2001; Koechlin et al. 2003; Koechlin and Summerfield 2007; Badre 2008) and more recently in lesion studies (Badre et al. 2009; Azuar et al. 2014). Although these studies provide evidence to support the existence of a set of frontal regions arranged in an anterior–posterior progression of functional specialization, spatial, and structural anatomical definitions of these regions are largely unknown.

Several methodological approaches that define the boundaries of functionally responsive brain regions recently became available (Caspers et al. 2013; Jbabdi and Behrens 2013).

Among these approaches, examining the nature of the input and output through the study of brain connectivity (i.e., connectomics) has emerged as one of the best solutions to segregate functional areas (Van Essen and Maunsell 1983; Mesulam 2005; Saygin et al. 2012; Zilles and Amunts 2015). Pursuant to this approach, diffusion-weighted imaging (DWI) tractography (Conturo et al. 1999) was employed to segregate *in vivo* functionally different, but anatomically adjacent, areas such as the supplementary motor area (SMA) and the pre-SMA (Johansen-Berg et al. 2004) or Brodmann areas 44 and 45 (Anwander et al. 2007) because they exhibit sharp changes in their connectivity. The results showed significant similarities between the brain regions that are defined by their connectivity (connectivity-based regions [CBR]) with those that are defined functionally (Jbabdi and Behrens 2013). However, such an approach has never been applied to the whole of the frontal lobes, partly due to difficulties in estimating *a priori* the number of sub-regions to be identified. While new, recent methodological attempts (Thiebaut de Schotten et al. 2014) have overcome this limitation by employing the principal component analysis (PCA) (Cattell 1966) framework, such an approach has never been applied to parcellate the whole of the frontal lobes. Further, reproducibility of the results across neuroimaging centers, acquisition parameters, populations, and individuals, as well as the functional specificity of the identified areas obtained using this new method remains to be assessed.

Preliminary evidence also suggests that the functional rostro-caudal organization of the frontal lobes would have an anatomical signature. For instance, although the most anterior portion of the human frontal lobes (i.e., Brodman area 10) shows a higher number of dendritic spines (Jacobs et al. 2001), lower myelination (Hopf 1956), and its relative size is the largest of all primates (Semendeferi et al. 2001), the remainder of the frontal lobes is more comparable to that of the ape, despite being larger than that of other primates and more distant relatives (Semendeferi et al. 2002). Hence, comparative anatomy studies suggest the expansion of the anterior frontal lobes along the phylogenic tree. Similarly, developmental studies have found that the ontogenesis of dendritic spines (Travis et al. 2005) and myelination (Flechsig 1920) are the latest to develop in the most anterior portion of the frontal lobe. These anatomical findings have been interpreted as the evolutionary changes that account for higher cognitive functions in humans (Passingham 1973). However, whether the differences in frontal architecture are limited only to the most anterior portion of the frontal lobes or whether these differences, as functional models suggest, follow a rostro-caudal gradient is currently unknown (Badre and D'Esposito 2009).

To explore the organization of the frontal lobes according to their architecture and connectivity, we employed DWI tractography based on Qball imaging (Tuch et al. 2005; Aganj et al. 2010) to segregate the whole frontal lobes in several connectivity-based areas in 2 independent datasets. Further, we used a database of meta-analysis of *f*MRI studies (Yarkoni et al. 2011) (http://neurosynth.org) to test the functional specialization and possible segregation across the identified regions. Finally, we built upon this result with recent developments in neuroimaging and postmortem histology by seeking biological markers for the rostro-caudal organization of the frontal lobes.

Materials and Methods

Subjects and MRI Acquisition

T1-weighted imaging, T2-weighted imaging, DWI, and resting state *f*MRI were obtained from 12 right-handed healthy controls (2 males and 10 females) from the Human Connectome Project (HCP) (http://www.humanconnectome.org, Q4 Release). Age of the participants ranged from 26 to 35 years.

Further, the dataset of 47 right-handed local healthy controls (24 males and 23 females) was gathered from previous studies (Aichelburg et al. 2016; Rojkova et al. 2016). The average age of the participants was 45 years (±14.79 years; range from 22 to 71 years). MRI included T1-weighted imaging and DWI.

Human Connectome Project Dataset

Data from the HCP dataset were acquired on a Siemens Skyra 3 T scanner at Washington University in St. Louis. The scanner was equipped with a customized body transmitter coil with 56 cm bore size (Van Essen et al. 2013)

Structural Imaging

An axial 3D T1-weighted imaging dataset covering the whole head was acquired for each participant (260 slices, voxel resolution = 0.7 mm^3, echo time (TE) = 2.14 ms, repetition time (TR) = 2400 ms, flip angle = 8°).

An additional 3D T2-weighted imaging dataset covering the whole head was acquired for each participant (260 slices, voxel resolution = 0.7 mm^3, TE = 565 ms, TR = 3200 ms, flip angle was variable).

DWI consisted in a total of 111 near-axial slices acquired with a multiband factor = 3 (Moeller et al. 2010; Ugurbil et al. 2013), isotropic (1.25 mm^3) resolution and coverage of the whole head with a TE = 89.5 ms and with a TR of 5520 ms. At each slice location, 18 images were acquired with no diffusion gradient applied. Additionally, 90 diffusion-weighted images were acquired, in which customized SC72 gradient were uniformly distributed in multiple Q-space shells (Caruyer et al. 2013). The acquisition of the diffusion weighting images was repeated 3 times with a b-value of 1000, 2000, and 3000 s mm^{-2}, respectively. Pairs of diffusion-weighted volumes were acquired with reversed right-to-left and left-to-right phase-encoding directions.

Resting State fMRI

During the resting state session, the room was darkened, participants were instructed to relax, keep their eyes open and fixate on a projected bright cross-hair on a dark background. Functional images were obtained using T2^*-weighted echo-planar imaging (EPI) with blood oxygenation level-dependent (BOLD) contrast. EPIs (TR/TE = 720/31 ms) comprised 72 axial slices acquired with multiband pulse (Feinberg et al. 2010; Moeller et al. 2010; Setsompop et al. 2012; Xu et al. 2012) covering the entire cerebrum (voxel size = 2 × 2 × 2 mm^3). Overall, 4 runs of approximately 15 minutes were acquired with oblique axial acquisitions alternated between phase encoding in a right-to-left (RL) direction in one run and phase encoding in a left-to-right (LR) direction in the other run.

Local Dataset

All local data were acquired on a Siemens 3 T VERIO TIM system equipped with a 32-channel head coil at Institute of Brain and Spine in Paris.

Structural Imaging

An axial 3D magnetization prepared rapid gradient echo (MPRAGE) dataset covering the whole head was also acquired for each participant (176 slices, voxel resolution = 1 × 1 × 1 mm^3, TE = 3 ms, TR = 2300 ms, flip angle = 9°).

DWI consisted in a total of 70 near-axial slices were acquired using a fully optimized acquisition sequence for the tractography of DWI, which provided isotropic ($2 \times 2 \times 2\,\text{mm}^3$) resolution and coverage of the whole head with a posterior–anterior phase of acquisition. The acquisition was peripherally-gated to the cardiac cycle (Turner et al. 1990; Conturo et al. 1995; Jones et al. 2002) with an TE = 85 ms. We used a TR equivalent to 24 RR. At each slice location, 6 images were acquired with no diffusion gradient applied. Additionally, 60 DWIs were acquired, in which gradient directions were uniformly distributed on the hemisphere with electrostatic repulsion. The diffusion weighting was equal to a *b*-value of 1500 s mm^{-2}.

DWI Preprocessing

Data was preprocessed using the default HCP preprocessing pipeline (V.2), which includes correction for susceptibility, motion, and eddy current distortions (Andersson et al. 2012; Sotiropoulos et al. 2013). Pairs of diffusion-weighted volumes were acquired with reversed right-to-left and left-to-right phase-encoding directions. This provides a pair of images with diffusion gradient applied with distortions going in opposite directions. From these pairs the susceptibility-induced off-resonance field was estimated using a method similar to that described in (Andersson et al. 2003) and corrected on the whole diffusion weighted dataset using the tool TOPUP as implemented in FSL (Smith et al. 2004). Finally, at each slice, diffusion-weighted data were simultaneously registered and corrected for subject motion and geometrical distortion using the tool EDDY as implemented in FSL.

For the local dataset, one supplementary image with no diffusion gradient applied but with reversed phase-encode blips was collected. This provides us with a pair of images with no diffusion gradient applied with distortions going in opposite directions. From these pairs the susceptibility-induced off-resonance field was estimated using a method similar to that described in (Andersson et al. 2003) and corrected on the whole diffusion weighted dataset using the tool TOPUP as implemented in FSL (Smith et al. 2004). Similarly to above at each slice, diffusion-weighted data were simultaneously registered and corrected for subject motion and geometrical distortion using the tool EDDY as implemented in FSL.

DWI Tractography

A tractography algorithm based on Qball imaging (20 000 samples, step length 0.5 mm, curvature threshold of 0.2) optimized for multishell (Tuch et al. 2005; Aganj et al. 2010; Sotiropoulos et al. 2011) was used to propagate streamlines from "seed" to "target" regions of interest (ROIs) situated in the white matter that was the closest to the grey matter. Within the white matter, water molecules diffuse more freely along axons than across them (Moseley et al. 1990), making it possible to obtain *in vivo* estimates of white matter fiber orientation by measuring the diffusivity of water molecules along different directions (Basser and Pierpaoli 1996; Basser et al. 2000). Conversely, water molecules diffuse more randomly within the grey matter because of its more complex organization, which includes neuronal cell bodies, glial cells, capillaries, dendrites, and axons. This uncertainty often leads to erroneous estimates of white matter fiber orientation and may flaw the tractography. Therefore, we created thin white matter ROIs, which were laid just below the grey matter ribbon. These ROIs were obtained using the intersection between white matter and the smoothed (2.5 mm full width at half maximum isotropic Gaussian kernel and using a lower threshold of 0.5) grey matter tissue types originally segmented with FSL FAST (24) applied to the MPRAGE dataset (Zhang et al. 2001). The result was then segmented into small ROIs of about 6 mm^2 (and 1 voxel thick) covering the entire white matter surface beneath the grey matter ribbon. In order to minimize the amount of variables representing false positives due to complex configuration such as kissing and fanning connections, additional ROIs were defined manually for the corpus callosum, the thalamus, and basal ganglia territories and used as target ROIs for the parcellation (Behrens et al. 2003; Rojkova et al. 2016).

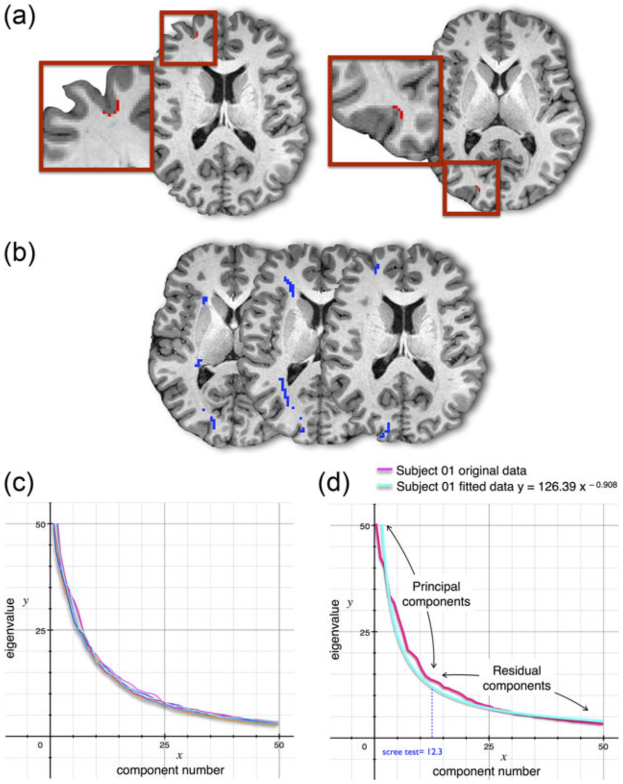

Figure 1. Tractography-based subdivision. (*a*) Left, example of a seed ROI used for tractography. Middle, example of a target ROI used for tractography. Right, example of the probabilistic tractography from the seed to the target. (*b*) Graph of the principal components (x) according to their eigenvalue sizes (y) for all subjects. Different colors are used for each subject. (*c*) Graph of the principal components (x) according to their eigenvalue sizes (y) for one representative subject. Original data is represented in purple and fitted data in cyan.

The skull was extracted from the MPRAGE dataset using Brain Extraction Tool (BET) provided in FMRIB Software Library (Smith 2002). The skull-stripped MPRAGE dataset and the ROIs were then registered to the b≈0 volume of the diffusion-weighted dataset using affine (FMRIB's Linear Image Registration Tool—FLIRT) deformation provided in FSL (http://fsl.fmrib.ox.ac.uk/fsl) (Smith et al. 2004)

Tractography-Based Parcellation

For the left and the right hemispheres, a frontal lobe mask was drawn on the Colin27 template (Holmes et al. 1998) provided in MRIcron (www.mccauslandcenter.sc.edu/mricro/mricron/) using surface anatomical landmarks. On the lateral surface, the central sulcus was used to delineate the separation from the frontal lobe and the parietal lobe. The lateral sulcus was identified to separate the temporal lobe from the frontal lobe. The left and the right frontal lobes were registered to the individual T1-weighted datasets using Advance Normalization Tools (ANTs, http://www.picsl.upenn.edu/ANTS/), which combine affine transformations with diffeomorphic deformations (Avants et al. 2008; Klein et al. 2009).

From each ROI in the left and right frontal masks, we seeded the tractography and recorded the proportion of streamlines that passed through each other ROI as a surrogate of the "probability of connection" to that zone (Fig. 1). This procedure has been shown to approximate the connectivity strength in animal tracer-injection studies (van den Heuvel et al. 2015). This "probability of connection" was corrected for size and the distance of the target using the following formula: ([number of tracks connecting the target ROI]/[number of voxel of the target ROI]) × (length of the tracks). For each participant, a "connectivity" matrix between frontal ROIs (seeds) and each other ROI of the ipsilateral hemisphere (targets) was derived from the results of the probabilistic tractography (Johansen-Berg et al. 2004). This matrix consisted of columns indexing the frontal ROIs, and rows that represented each ROI in the ipsilateral hemisphere.

Statistical analysis was performed using SPSS software (SPSS, Chicago, IL). Each value of the "connectivity" matrix obtained from the tractography was converted into Z-scores and entered into a PCA using a covariance matrix and quartimax rotation (with a maximum of 50 iterations for convergence) in order to estimate the number of principal components to extract for each subject (Fig. 1). We plotted the components according to eigenvalues (y) and applied a scree test to separate the principal from residual components (Cattell 1966). The data was fitted to a power curve and the inflexion point was extracted using a homemade routine written in Matlab 7.8 (http://www.mathworks.com). On average, 12.54 (±.29) and 12.34 (±.45) main components were obtained for the left and the right frontal lobes of the HCP dataset.

A subsequent PCA was performed similarly with a fixed number of 12 components to be extracted. The result was used to group together ROIs of the frontal lobes in 12 clusters (referred as CBRs), which corresponded to the twelve components extracted from the PCA. Each cluster was extended to the nearest adjacent cortex combining a 5 mm full half width maximum smoothing with the command find_the_biggest in FSL.

For each lobe, the 12 clusters were registered to the Colin27 template using the inverse of the affine transformations and diffeomorphic deformations estimated with ANTs (Avants et al. 2007; Klein et al. 2009; Tustison and Avants 2013) to register the left and the right frontal lobes with the individual MPRAGE datasets. The individual registered clusters were overlapped to produce averages. These average clusters were gathered in a single file with the command find_the_biggest in FSL, which displayed clusters with the highest probability of overlap (Behrens et al. 2003). Display of axial brain slices was performed using MRIcron (http://www.mccauslandcenter.sc.edu/mricro/mricron). 3D rendering of the brains was calculated using the T1 pipeline in BrainVISA. The overall visualization and screenshots were performed using the software anatomist (http://brainvisa.info). In order to cross validate our results in a different population connectivity-based subdivision of the frontal lobe was applied to the local dataset following the exact same steps. Similarly we obtained 12 CBR with a high similarity with subdivision of the HCP subjects' frontal lobe.

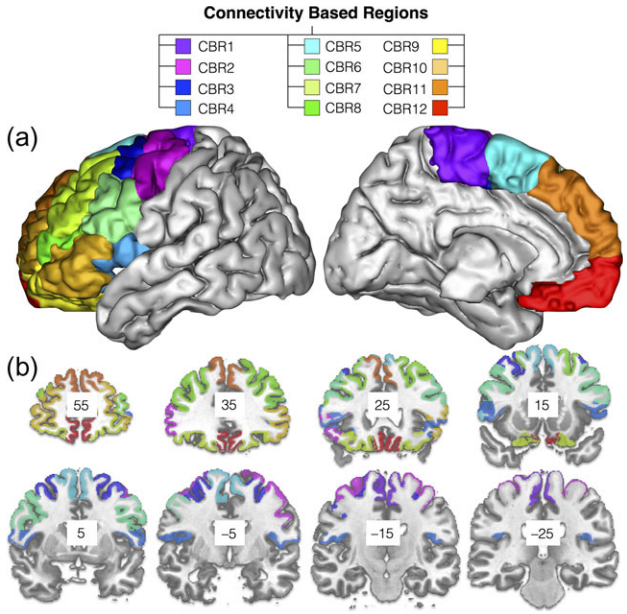

Figure 2. Brain regions of the frontal lobes defined using anatomical connectivity. (*a*) Lateral and medial views. (*b*) Montreal Neurological Institute stereotaxic coronal sections.

*f*MRI Meta-Analysis

Functional segregation across the identified CBRs was further investigated using the decode tool provided in Neurosynth (Yarkoni et al. 2011; Gorgolewski et al. 2015; Gorgolewski et al. 2016) (http://www.neurosynth.org). Each region was compared with functional activations related to 2912 different terms. The result was subsequently converted into Z-score in order to reveal the function most likely activated in the CBRs. For each CBR, we kept the most associated functional term and reported it in Figure 5*a*. The maps associated with each of these functional terms were built in Neurosynth and are displayed on Figure 6. We ran spatial correlations between these functional maps and the CBRs, using a mask of the frontal lobe. Correlation coefficients are provided in Figure 5*b*.

Cortical Thickness

A registration-based method (Diffeomorphic Registration based Cortical Thickness, DiReCT) was employed to estimate the cortical thickness (Das et al. 2009) from the T1-weighted imaging dataset. The first step of this method consists in creating a 2-voxel thick sheet, one lying just between the grey matter and the white matter and the second laying between the grey matter and the cerebrospinal fluid. Then, the grey/white interface is expanded to the grey/cerebrospinal fluid interface using diffeomorphic deformation estimated with ANTs (Avants et al. 2007; Klein et al. 2009; Tustison and Avants 2013). The registration produces a correspondence field that allows an estimate the distance between the grey/white and the grey/cerebrospinal fluid interfaces, and thus cortical thickness. This approach has good scan-rescan repeatability and good neurobiological validity as it can predict with a high statistical power the age and gender of the participants (Tustison et al. 2014). FSLstats was employed to extract cortical thickness profile for each CBR defined at the individual level.

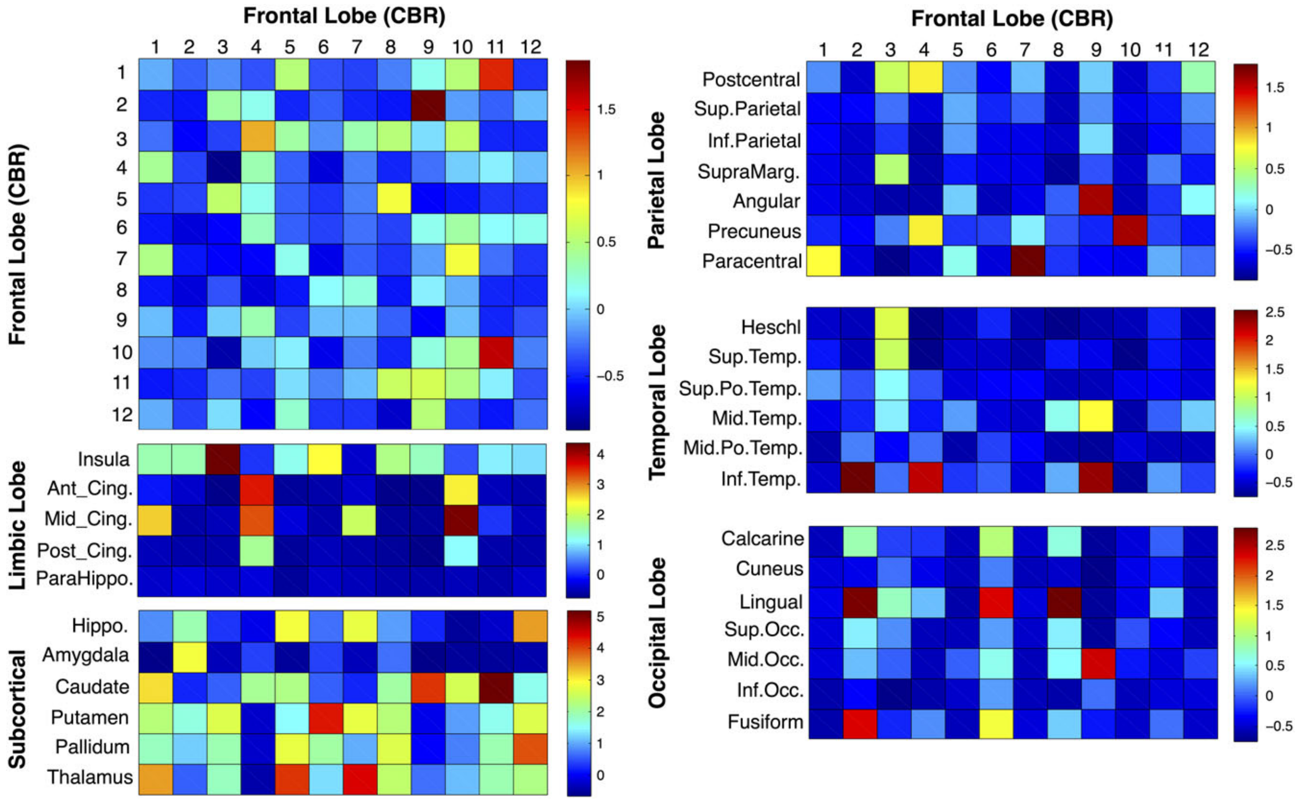

Figure 3. *Z-score of the distribution of the structural connections emerging from each CBR. Ant, anterior; Mid, middle; Post, posterior; Cing., cingulate; ParaHippo., parahippocampic gyrus; Hippo, hippocampic gyrus; Sup, superior; Inf, inferior; Supramarg, supramarginal gyrus; Temp, temporal; Mid Po, middle posterior; Occ, occipital.*

Connectivity-Independent Anteroposterior Parcellation

We additionally performed the same correlation analyzes on a parcellation of the frontal lobe obtained without considering its anatomical connectivity. Specifically, we characterized each frontal voxel uniquely on the basis of its anatomical location, in terms of x, y, and z coordinates. The matrix of anatomical coordinates of the frontal region was then fed into the k-means clustering implementation provided in Matlab. We asked the algorithm to parcellate the frontal cortex in 12 clusters, to enable the comparison with the 12 connectivity-based CBR. This allowed us to compare CBRs to connectivity-independent clusters and to assess the functional, architectural, and structural specificity of CBRs' properties.

T1/T2 Myelin Quantification

In this section we took advantage of the opposite covariance of myelin with T1w and T2w intensities (Glasser and Van Essen 2011). Lipids, water concentrations (free and myelin bound) as well as iron strongly increased T1w signal and decreased T2w signal. Within the grey matter, myelin, and iron are well co-localized, particularly due to the iron contents of oligodendrocytes (Connor and Pinero 2005). Thus, T1w/T2w ratio can be employed as a surrogate for the quantification of local cortical grey matter myelin content.

T1w and T2w images were registered using FSL FLIRT (Jenkinson et al. 2002). Susceptibility-induced artifacts affect T1w and T2w data differently. Therefore T2w image was further registered and resampled using a spline interpolation algorithm as provided by FSL's FNIRT (Anderson et al. 2007). Bias field signal is a low-frequency and very smooth signal that produces local inhomogeneity MRI measures. However, it is

Table 1 Summary of the measures employed in the analyzes

	CBR	Center of gravity (y)	Cortical Thickness	T1/T2 myelin ratio	Cell bodies staining	Entropy
LEFT	CBR1	102.541	2.830	1.900	198.055	9938.665
	CBR2	112.801	2.805	1.886	214.630	9255.855
	CBR3	124.969	3.082	1.847	211.291	10770.922
	CBR4	130.423	3.331	1.883	208.112	11309.739
	CBR5	135.173	3.312	1.822	205.532	12324.478
	CBR6	136.461	3.151	1.838	217.056	10877.946
	CBR7	165.657	3.596	1.786	231.257	12070.867
	CBR8	154.802	3.381	1.775	220.981	12780.704
	CBR9	164.700	3.653	1.798	207.008	–
	CBR10	164.702	3.417	1.792	224.580	11473.906
	CBR11	172.211	3.520	1.736	225.706	13665.498
	CBR12	169.977	3.824	1.770	209.520	–
RIGHT	CBR1	99.393	2.687	1.890	197.959	10069.207
	CBR2	125.595	2.847	1.790	196.573	9894.293
	CBR3	122.613	2.986	1.778	199.786	10581.950
	CBR4	126.005	3.280	1.780	201.456	10684.590
	CBR5	128.588	3.221	1.773	207.223	10741.482
	CBR6	134.838	2.889	1.734	199.459	11960.587
	CBR7	147.007	3.126	1.709	201.826	12063.398
	CBR8	161.605	3.256	1.676	202.843	12148.622
	CBR9	161.023	3.711	1.711	197.353	–
	CBR10	176.365	3.469	1.673	217.024	10689.048
	CBR11	170.117	3.318	1.664	229.131	13066.522
	CBR12	173.132	3.930	1.693	223.193	–

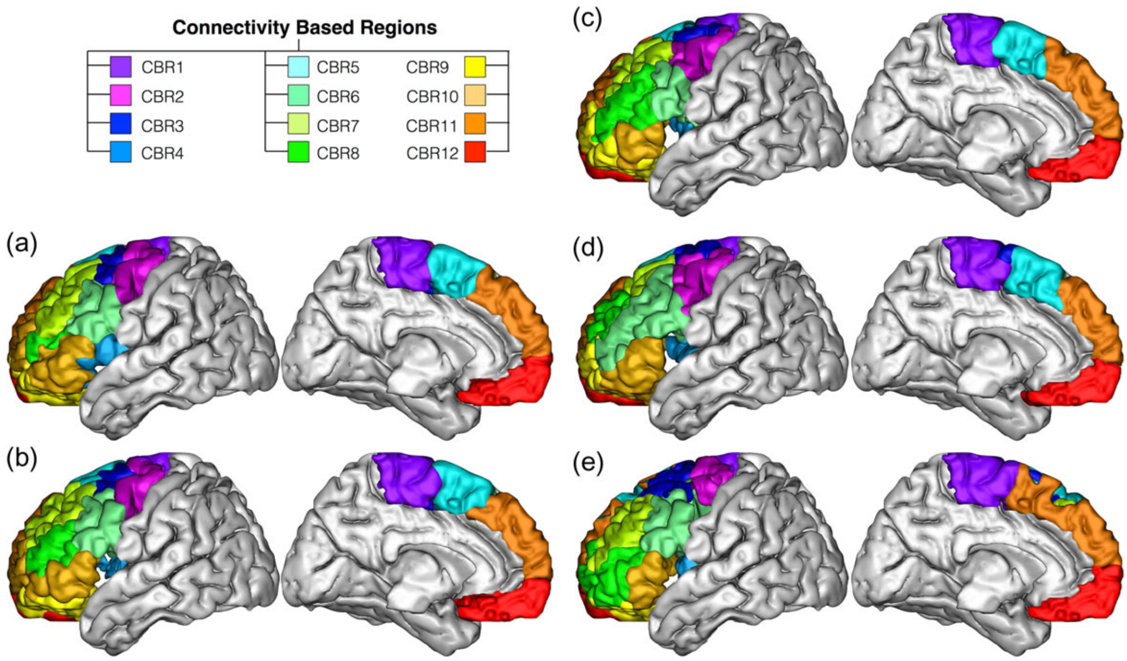

Figure 4. Reproducibility across datasets (*a*) Human Connectome Project and (*b*) local dataset tractography-based subdivision of the whole frontal lobe; (*c–e*) 3 representative participants (respectively c, best case; d, average case; and e, worst case).

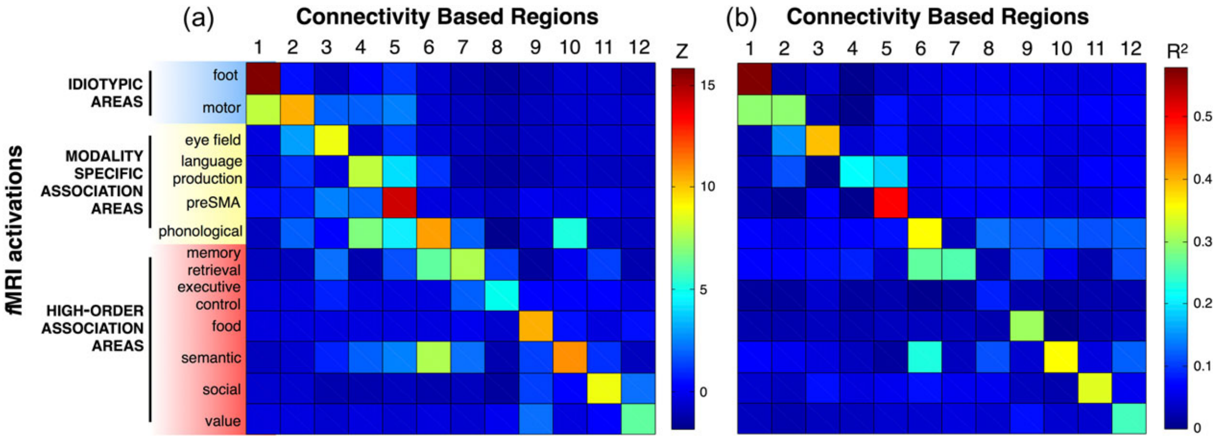

Figure 5. Function most likely activated for each CBR. (*a*) Z-score indicate the likeliness for each CBR to be activated for the term indicated in ordinate (compared with 2912 other term-related activations provided in Neurosynth, http://www.neurosynth.org). (*b*) Spatial correlations between each CBR and functional maps (illustrated in Figure 5). "foot": lower limb primary motor area, "motor": upper limb motor area, "eye field": frontal eye field, "language production": broca's area, "pre-SMA": pre-supplementary motor area, "phonological:" phonological processing, "semantic": semantic knowledge, "social": social functions, "value": value-based behavior.

important to note that division of the T1w image by the aligned T2w image mathematically cancels the signal intensity bias, therefore there is no need for bias correction when carrying on T1w/T2w analyzes (Glasser and Van Essen 2011). T1w/T2w contrast was finally masked with the grey matter ribbon calculated during the cortical thickness estimation to avoid any white matter signal contamination. The final images were checked individually and were satisfactory in all participants. FSLstats was then used to extract the myelin estimation profile for each CBR defined at the individual level.

BigBrain Cell Body Density Quantification

BigBrain (Amunts et al. 2013) is a high-resolution (20 µm) postmortem brain, stained for cell bodies (Merker 1983) and registered to the 2009 ICBM 152 Nonlinear atlas (Fonov et al. 2011). This material is publicly available at https://bigbrain.loris.ca.

In order to extract average cell body density for each CBRs as defined in 1.1.4, we first registered the Colin27 template to the 2009 ICBM 152 Nonlinear template using ANTs and applied this deformation to our group-level CBR. FSLstats was then used to extract myelin estimation profile for each CBR defined at the group level.

Resting State *f*MRI Entropy Estimation

The four runs of resting state functional MRI were at first corrected for gradient distortion using FSL's FUGUE, then a motion correction (MCFLIRT) procedure was applied in order to remove any motion related artifact within each run. The 2 resting state *f*MRI runs were acquired with right-to-left phase-encoding directions and 2 with left-to-right phase-encoding directions. This provided runs with distortions going in opposite directions. From these pairs the susceptibility-induced off-resonance field was estimated using a method similar to that described in (Andersson et al. 2003) and corrected on the whole diffusion-weighted dataset using the tool TOPUP as implemented in FSL (Smith et al. 2004). The corrected runs were then registered to the T1-weighted individual data using FSL's FLIRT and then registered to the ICBM 152 Nonlinear atlas using FSL's FNIRT. Individual CBR were registered to the ICBM 152 Nonlinear atlas using the same deformation field as above using a nearest-neighbor interpolation. Data were further corrected for movement, cardiac, and respiratory artifact using FSL FIX, which auto-classify ICA components and regress out their signal from the resting state data (Griffanti et al. 2014; Salimi-Khorshidi et al. 2014). FSLstats was then employed to extract the resting state *f*MRI entropy for each individual CBR.

Note that some of the frontal ventral areas of the resting state *f*MRI remained affected by unrecoverable susceptibility artifacts at the end of processing. Therefore we had to exclude CBR 9 and 12 from the mean entropy analysis.

Statistics

SPSS software (SPSS, Inc., Chicago, IL, USA) was employed to carry on Pearson correlation analyzes between the variables presented in Table 1. To assess similarity between the HCP and the local dataset, as well as CBRs and functional activation maps, voxel to voxel Pearson's correlation was carried on using FSLcc. For each CBR, a lateralization index was calculated for the volume, thickness, T1/T2 ratio, and entropy data according to the following formula:

$$\text{Lateralization index} = \frac{(\text{Right CBR} - \text{Left CBR})}{(\text{Right CBR} + \text{Left CBR})}.$$

The statistical significance of the degree of lateralization was determined using a one-sample *t* test for each CBR. Only the results that survived the Bonferroni correction ($P < 0.001$) are reported.

Results

A PCA (Fig. 1) applied to the measure of the brain anatomical connectivity in 12 healthy participants issued from the HCP dataset (http://www.humanconnectome.org) identified 12 CBRs in the left and right frontal lobes (maps displayed in Figure 2 also available on demand, contact michel.thiebaut@gmail.com). There was no significant difference in volume between the left and right CBRs.

Anatomical connectivity for each CBR is summarized in Figure 3 and demonstrates that each of the CBRs showed a specific pattern of connections with the rest of the brain with a clear dominance for cortico-subcortical connections.

These results were replicated in a second dataset ($n = 47$ participants), producing a frontal division almost identical to the one obtained with the HCP dataset (Pearson correlation $R^2 = 0.96$, Fig. 4*a* and *b*). This suggests that the number of CBRs which can be identified in the frontal lobes, as well as their boundaries, are reproducible across populations, and that they are driven by the structural connectivity of the brain rather than, to some extent, the resolution or the quality of the DWI data. Note that the frontal division at the individual level also showed clear similarities with the group (mean Pearson correlation across participants $R^2 = 0.919$, Fig. 4*c*–*e*), with some differences that may reflect individual specificity.

We examined the functional significance of these CBRs using Neurosynth (www.neurosynth.org). *Z*-scores in Figure 5*a* indicate the likelihood for a CBR to be activated more by specific term-related activations, in comparison to 2912 other term-related activations. R^2 scores in Figure 5*b* indicate the resemblance between each CBR and the maps of each term-related functional activation.

The results indicate a clear functional segregation across the CBRs, which successfully corresponded to well-known functional areas including the motor areas (CBR 1 and 2; *Z*-score = 15.84; $R^2 = 0.58$ and *Z*-score = 10.43; $R^2 = 0.29$ respectively), frontal eye field (CBR3; *Z*-score = 8.86; $R^2 = 0.39$), Broca's area (CBR4; *Z*-score = 7.95; $R^2 = 0.21$), and pre-SMA (CBR5; *Z*-score = 14.25; $R^2 = 0.5$).

Further, it also divided more anterior portions of the frontal lobes into areas classically associated with phonological processing (CBR6; *Z*-score = 10.81; $R^2 = 0.36$), memory retrieval (CBR7; *Z*-score = 7.64; $R^2 = 0.26$), executive control (CBR8; *Z*-score = 4.87; $R^2 = 0.09$), food (CBR9; *Z*-score = 10.5; $R^2 = 0.3$), semantic knowledge (CBR10; *Z*-score = 11.06; $R^2 = 0.36$), social functions (CBR11; *Z*-score = 8.88; $R^2 = 0.34$) and value-based behavior (CBR12; Z-score = 6.25; $R^2 = 0.25$) related tasks. Note that although CBRs had a good specificity for term-related functional activations, there was a moderate overlap between the CBR and the term-related activation maps for high-order cognitive functions (Fig. 6–7).

Overall the CBRs were organized functionally on a rostro-caudal axis from the most complex high-order association areas to the simplest idiotopic areas (Fig. 5) (Mesulam 2000).

We further assessed whether an architectural gradient would support the rostro-caudal functional organization across the areas identified in the frontal lobes in the high-resolution HCP dataset. Cortical thickness analyzes (Das et al. 2009; Tustison et al. 2014) revealed that anterior CBRs were thicker than posterior CBRs. This result was highly significant at the group level (Fig. 8*a* left hemisphere $R^2 = 0.856$; $P < 0.001$; right hemisphere $R^2 = 0.642$; $P = 0.002$) as well as at the individual level (Fig. 8*b*). Further, CBRs 6 ($t_{(11)} = -5.147$; $P < 0.001$) and 7 ($t_{(11)} = -5.883$; $P < 0.001$) were significantly thicker in the left than in the right hemisphere.

The strength of the individual correlation between cortical thickness and the postero-anterior position was significantly higher for the CBRs than that of similar analyzes obtained in a connectivity-independent postero-anterior parcellation ($t_{(11)} = 3.782$; $P = 0.003$), thus indicating the specificity of the architectural gradient to the CBRs identified.

Measures of cortical thickness are contingent to several factors including myelination, cells density, or intrinsic synaptic and dendritic complexity (Wagstyl et al. 2015; Zilles and Amunts 2015).

Myelin content in the cortex can be quantified using a ratio between T1-weighted (T1w) and T2-weighted (T2w) MRI (Glasser and Van Essen 2011). Figure 9*a* indicates that cortical myelin content is progressively lower from posterior to anterior CBRs in the left hemisphere ($R^2 = 0.880$; $P < 0.001$). These results were further replicated in the right hemisphere ($R^2 = 0.900$; $P < 0.001$). Further CBRs 4 ($t_{(11)} = -5.466$; $P < 0.001$), 6 ($t_{(11)} = -5.837$; $P < 0.001$), 8 ($t_{(11)} = -5.520$; $P < 0.001$), 10 ($t_{(11)} = -5.738$; $P < 0.001$) and 12 ($t_{(11)} = -4.882$; $P < 0.001$) were significantly more myelinated in the left than in the right hemisphere.

Cell bodies can be identified using silver staining (Merker 1983). Density of the cell bodies for each CBR was extracted

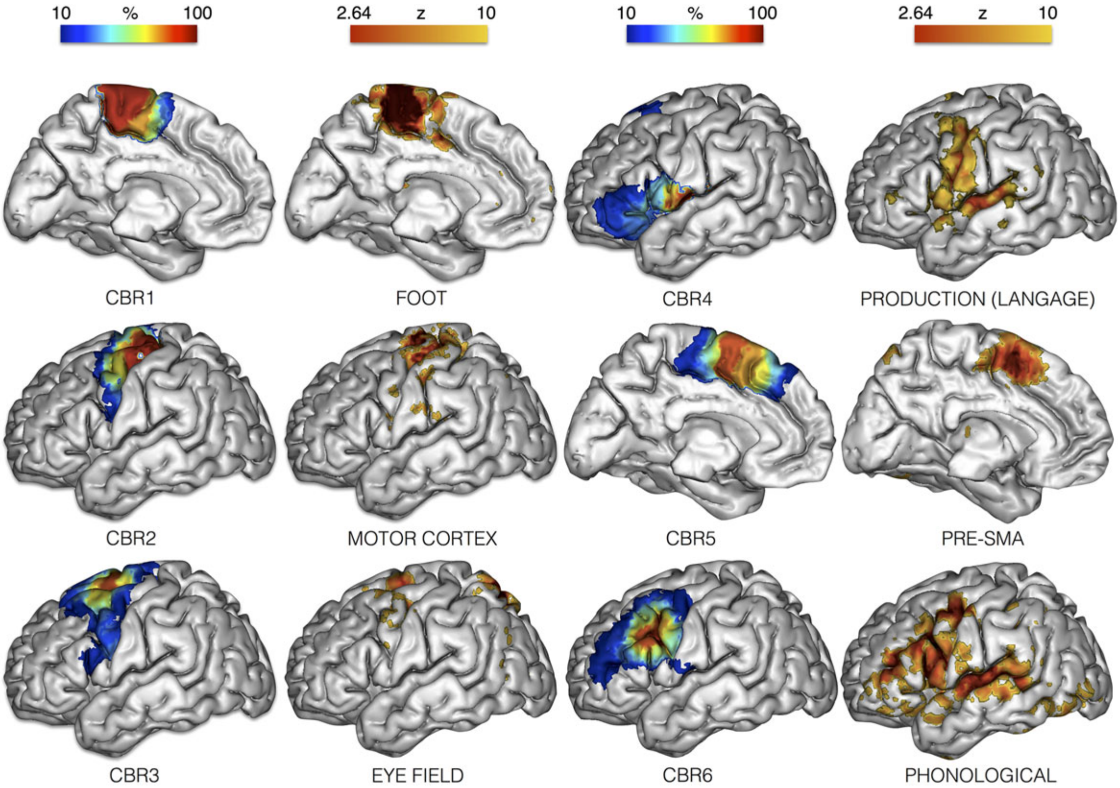

Figure 6. Side-by-side comparison between the CBR1-6s' percentage maps and task-related *f*MRI maps drawn from meta analyzes in Neurosynth (http://www.neurosynth.org).

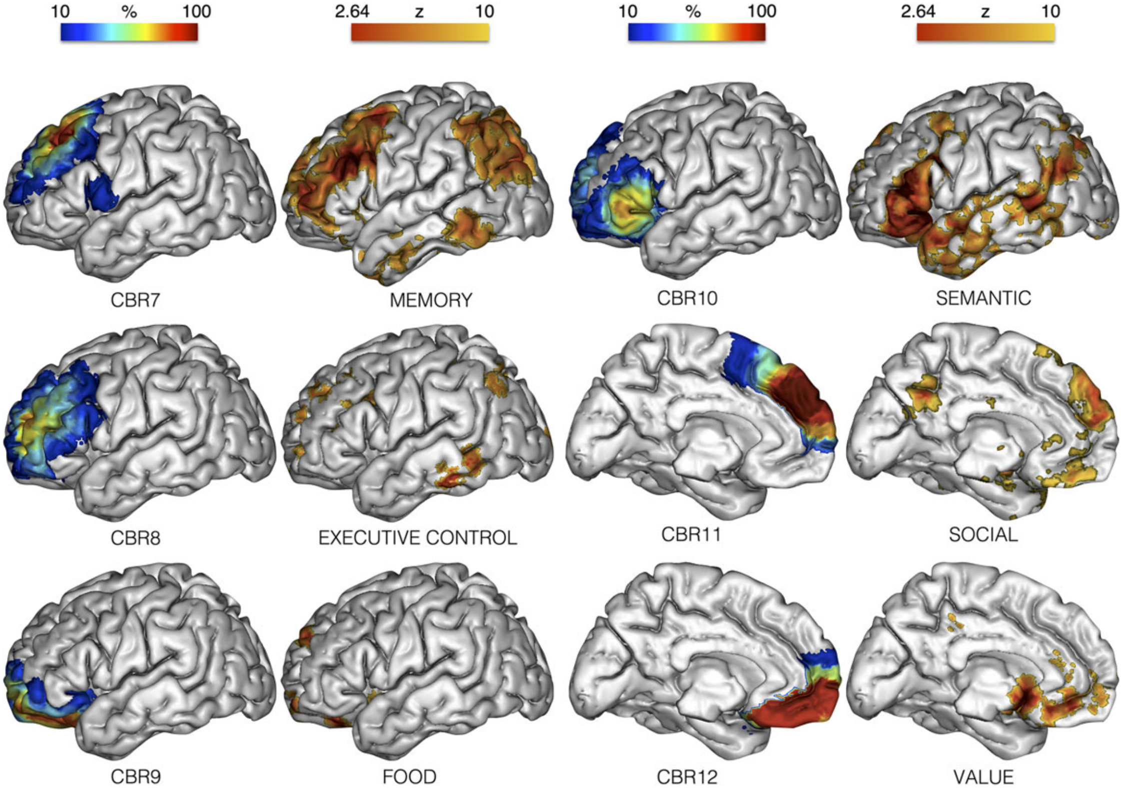

Figure 7. Side-by-side comparison between the CBR7-12s' percentage maps and task-related *f*MRI maps drawn from meta analyzes in Neurosynth (http://www.neurosynth.org).

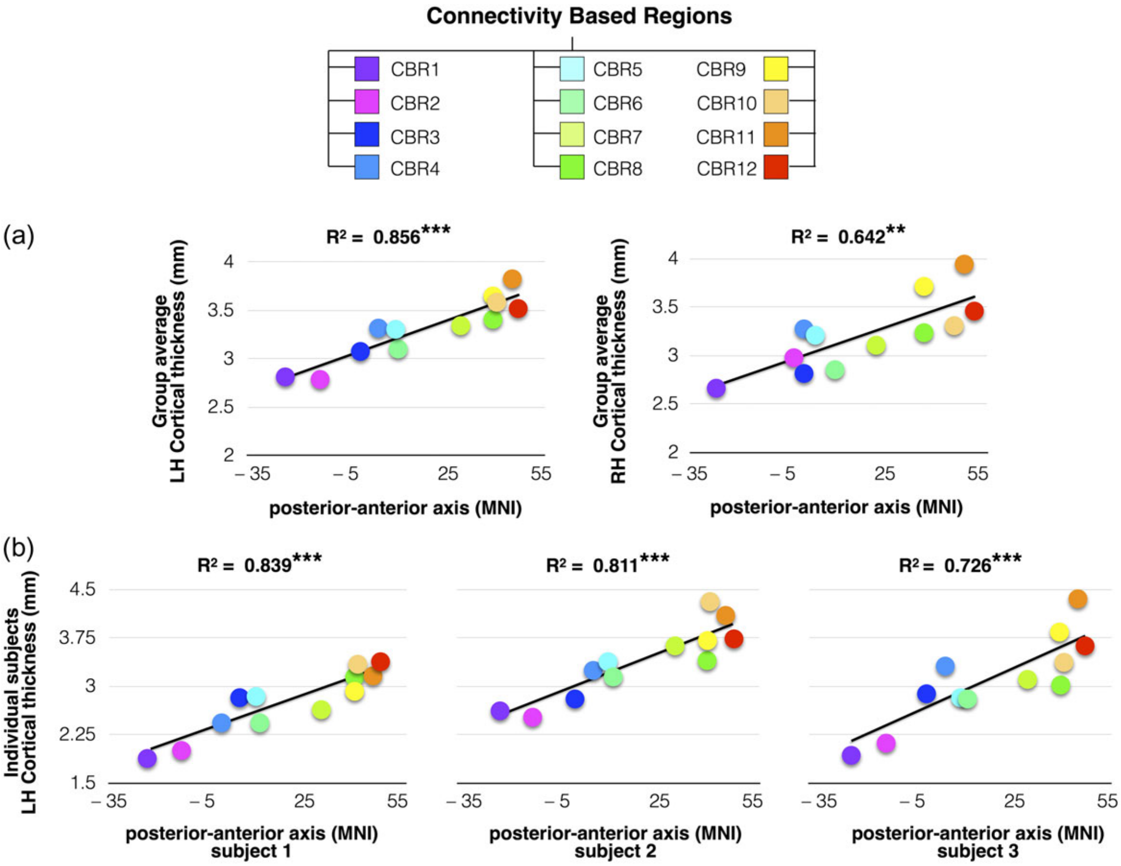

Figure 8. Correlations between the posterior–anterior position of each region's centroid and cortical thickness (*a*) at the group level (*b*) at the individual level in three participants. LH, left hemisphere; RH, right hemisphere; MNI, Montreal Neurological Institute (http://www.bic.mni.mcgill.ca). *$P < 0.05$, **$P < 0.01$, ***$P < 0.001$.

from a single postmortem brain issued from the BigBrain Loris database (Amunts et al. 2013) (https://bigbrain.loris.ca). Note that using this contrast, an increase in cell body density will correspond to a darker staining. Results illustrated in Figure 9*b* and 9*c* revealed a posteroanterior gradient of cell body density with anterior CBR containing smaller cells that are less densely packed than in posterior CBRs of both left ($R^2 = 0.372$; $P = 0.035$) and right hemispheres ($R^2 = 0.477$; $P = 0.013$). These results, therefore, discarded the myelination and the densely-packed cells hypotheses as an explanation for the thicker CBRs. The use of a single brain for the quantification of cell density did not allow for a statistical comparison between the left and right hemispheres.

To address the possibility of more connective properties in anterior regions, entropy measures of the resting state *f*MRI were employed to quantify the complexity of brain dynamics in each CBR as a surrogate for intrinsic synaptic and dendritic complexity (Sokunbi et al. 2011; Yao et al. 2013). The results revealed that anterior CBRs have a higher entropy than posterior CBRs for the left and right hemispheres (Fig. 9*d*; $R^2 = 0.689$; $P = 0.003$ and $R^2 = 0.426$; $P = 0.041$, respectively). There was no significant difference in entropy between the left and right CBRs. Finally, entropy accounted for approximately 50% ($R^2 = 0.461$; $P = 0.001$) of the variance in CBRs' thickness.

Discussion

In this study we used DWI tractography to divide the frontal lobes in areas defined by their structural connectivity and in coherence with functional specificity, and employed multimodal imaging to further characterize these areas. Several findings emerge from our work. First, the frontal lobes can be divided into 12 regions defined by their anatomical connectivity consistently across datasets and participants. Secondly, these areas showed clear functional specificity as defined by a meta-analysis performed on a wide number of fMRI studies. Thirdly, the CBRs were organized linearly along an anteroposterior axis according to their cortical thickness, myelination, cell body density, intrinsic synaptic & dendritic complexity. Finally, strong hemispheric asymmetries were also revealed in the thickness and in the myelination of several CBRs.

PCA statistical framework applied to tractography results successfully integrated structural connectivity information, producing a division of the frontal lobe that was reproducible between 2 datasets and reliable between individuals. This suggests that our method to identify frontal CBRs, including their boundaries, is reproducible across populations/individuals, and is driven by the structural connectivity of the brain rather than, to some extent, the resolution or the quality of the DWI data. As compared with the previous attempts to divide the frontal lobes based on structural connectivity, the PCA method successfully identified the M1/SMA and the Pre-SMA (CBR1 and CBR5) (Johansen-Berg et al. 2004; Li et al. 2013), Brodman areas 44 and 45 (CBR4 and posterior part of CBR10) sub-portion of Broca's area (Anwander et al. 2007), as well as dorsal (CBR3) and ventral (CBR6) premotor cortices (Tomassini et al. 2007) with high reproducibility across datasets and participants

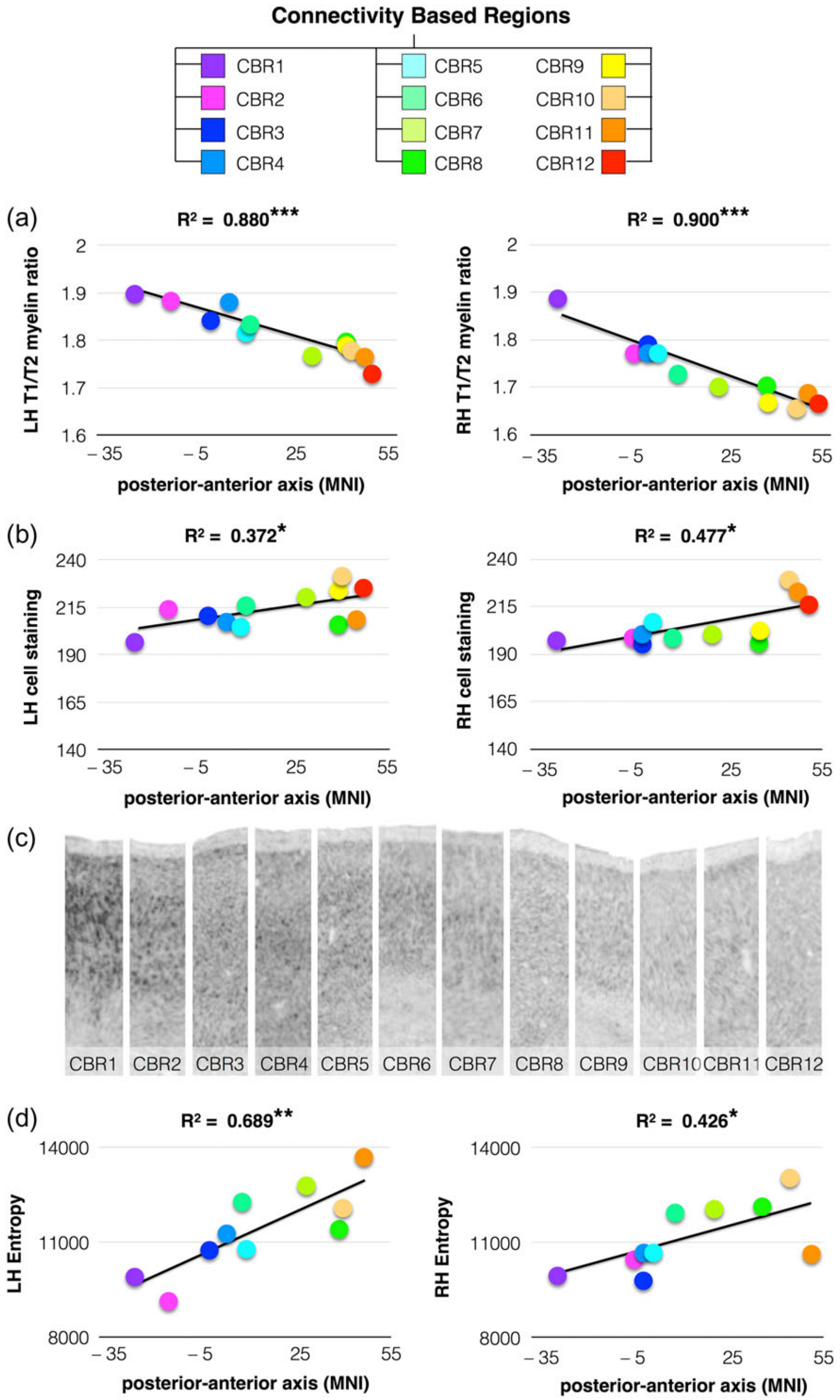

Figure 9. Correlations between the postero-anterior position of each CBR and (*a*) T1w/T2w myelin ratio. (*b*) Silver staining of cortical cell bodies (decreased values indicate an increase in the staining of tissue). (*c*) An example of cortical cell bodies staining for each CBR (http://bigbrain.loris.ca) (*d*) Correlations between the postero-anterior position of each CBR and functional magnetic resonance imaging entropy. LH, left hemisphere; RH, right hemisphere. $^{*}P < 0.05$, $^{**}P < 0.01$, $^{***}P < 0.001$.

(Klein et al. 2007). Similarly, the precentral gyrus was divided into 4 sub-portions (CBR1, CBR2, CBR4, and CBR6) (Schubotz et al. 2010), although some of these regions extended to the premotor cortex. PCA also divided the ventral prefrontal cortex, as previously suggested from animal studies into an orbital lateral (CBR9) and a medial area (CBR12) functioning as a sensory-visceromotor system, in particular with regard to eating (Carmichael and Price 1996; Ongur and Price 2000). These areas extended to the frontal pole, the latter being divided into an orbital (CBR9) a lateral (CBR11) and a medial region (CBR12) (Liu et al. 2013). Our approach, however, identified a smaller number of areas in the dorsolateral prefrontal cortex than previously reported (Sallet et al. 2013). Differences in the methods used to extract the optimal number of regions likely explain this difference. Future research will be required to evaluate whether the data-driven scree-test approach is more reliable than the operator-dependent *k*-mean clustering iteration. Overall, our method well replicated previous work on tractography-based parcellation, with the added advantage of being applicable to larger brain areas than classical approaches.

The 12 CBRs identified in the frontal lobes showed clear functional specificity as defined by functional MRI. This finding is a vivid illustration of the concept according to which the functions of an area can be defined by the nature of its structural connections (Van Essen and Maunsell 1983; Mesulam 2005; Zilles and Amunts 2015) and delivers further evidence to support the use of diffusion imaging tractography to understand brain functioning. Using tractography to divide the brain may then provide a better understanding of the normal organization of the brain and its dysfunction. For instance, according to the results, the frontal eye-field (CBR3) is at the interplay between areas whose damage leads to a severe impairment of visual awareness (i.e., visual neglect) such as striatum (Karnath et al. 2002), thalamus (Watson et al. 1981), supramarginal gyrus (Thiebaut de Schotten et al. 2005), superior temporal gyrus (Karnath et al. 2001). Similarly, the frontal pole (BA 10) has consistently shown to be involved in the highest level of cognitive abilities, such as relational reasoning (Smith et al. 2007; Volle et al. 2010; Vartanian 2012; Hobeika et al. 2016; Urbanski et al. 2016), combining of remote information (Gonen-Yaacovi et al. 2013), coordinating goals and sub-goals (Koechlin et al. 1999; Kroger et al. 2002), multitasking (Burgess et al. 2009; Volle et al. 2011), and decision-making (Fellows 2012; Domenech and Koechlin 2015). The results suggest this area should be at least divided into a lateral (CBR10) and a medial (CBR12) sub-portion according to their input and output. Interestingly, recent evidence revealed that medial and lateral portions of the frontal pole have a different cytoarchitecture (Bludau et al. 2014) as well as separate functions (Gilbert et al. 2010; Volle et al. 2010). The nature of structural connectivity, therefore provide new insights that strengthen our understanding of the mechanisms that support functional specialization, as well as further understanding of neurological pathologies.

Interestingly, CBRs were organized functionally on a rostrocaudal axis from the most complex high-order association areas to the simplest idiotopic areas (Mesulam 2000). The quantification of magnetic resonance and histological biomarkers also revealed that the identified frontal regions have a hierarchical linear anatomical organization. Anterior regions are thick, less myelinated, and populated by small and distant cells whereas posterior regions are heavily myelinated and populated by densely packed larger neurons. Greater myelination correlates with conduction speed (Waxman and Bennett 1972), which may impact the processing speed of frontal areas. Larger distances between the cells of the anterior frontal regions can be interpreted as a consequence of larger numbers of dendritic spines and synapses, which has led to our observation of a significant increase in *f*MRI entropy. Our report, therefore, suggests that as information processing travels more anteriorly in the frontal lobes, it should also increase its complexity and decrease its celerity linearly. This result complements the findings of electrophysiology and functional studies (Badre and D'Esposito 2009) by providing an anatomical signature to the functional rostrocaudal organization of the frontal lobes.

Several asymmetries were also reported. For instance CBR6, which is classically activated during phonological tasks, was thicker and more myelinated in the left hemisphere. This asymmetry might relate to the dominance of the left hemisphere for language (Broca 1863; Geschwind and Galaburda 1985; Mazoyer et al. 2014) and requires further investigation in order to determine whether it can be used as a biomarker for language lateralization. Additional areas showed a stronger myelination in the left hemisphere. Preliminary evidence already demonstrated an earlier myelination in left than the right hemisphere (Deoni et al. 2011), and the present findings suggest that hemispheric differences may persist into the adult age.

In this study, indices of structural connectivity strength were extracted from probabilistic tractography. Stricto sensu probabilistic tractography estimates the mathematical confidence of a white matter pathway for a given dataset (Jones 2008, 2010; Jones et al. 2013) and not structural connectivity strength. We tried to circumvent this issue using a *Z*-score normalization of the number of streamlines (Thiebaut de Schotten et al. 2014) emerging from each region of interest. Hence *Z*-scores indicate the pattern of structural connectivity for each region of interest, rather than its absolute strength.

We employed an *f*MRI meta-analytic approach (http://www.neurosynth.org) to better characterize the function for each CBR. *f*MRI meta-analytic approaches have limitations, such as publication biases, which should be, and have been, considered when interpreting results (Jennings and Van Horn 2012). Moreover, the functional activation and the CBRs were based on 2 distinct populations. Further research will be required to directly explore the relationship between CBRs and the BOLD changes associated with specific functions and their inter individual variability. This work provides a new framework, and subsequently, new hypotheses to test regarding the anatomical bases of frontal functions.

Overall, the current results demonstrate that the functioning of the frontal lobe is associated with clear anatomical signatures, and that notwithstanding limitations, that the exploration of structural connections is paramount to the understanding of brain function and dysfunction. For instance, recent evidence demonstrated abnormal structural connectivity in the frontal lobes in autism spectrum disorder (Catani et al. 2016; Ecker et al. 2016). Tractography-based subdivision may demonstrate a singular division associated with autism spectrum disorder or reveal finer differences in the CBR's anatomical features such as cortical thickness variation, myelin distribution, and connectional complexity. Hence, further research should investigate whether these measures could help to account for the large inter-individual variability by providing a personalized quantification of functionally characterized areas in the frontal lobe. This approach may strengthen the prediction or diagnosis of neurodevelopmental and neurodegenerative disorders (Le Ber et al. 2006; Ecker et al. 2015).

Notes

We thank Lauren Sakuma for useful discussions. Data was provided in part by the Human Connectome Project, WU-Minn Consortium (Principal Investigators: David Van Essen and Kamil Ugurbil; 1U54MH091657) funded by the 16 NIH Institutes and Centers that support the NIH Blueprint for Neuroscience Research; and by the McDonnell Center for Systems Neuroscience at Washington University. The BigBrain dataset is the result of a collaborative effort between the teams of Dr Katrin Amunts, Dr Karl Zilles (Forschungszentrum Jülich) and Dr Alan Evans (Montreal Neurological Institute). Additional support comes from the "*Agence Nationale de la Recherche*" [grants number ANR-09-RPDOC-004-01 and number ANR-13-JSV4-0001-01] and from the Fondation pour la Recherche Médicale (FRM). The research leading to these results received funding from the program "*Investissements d'avenir*" ANR-10-IAIHU-06.

References

Aganj I, Lenglet C, Sapiro G, Yacoub E, Ugurbil K, Harel N. 2010. Reconstruction of the orientation distribution function in single- and multiple-shell q-ball imaging within constant solid angle. Magn Reson Med. 64:554–566.

Aichelburg C, Urbanski M, Thiebaut de Schotten M, Humbert F, Levy R, Volle E. 2016. Morphometry of left frontal and temporal poles predicts analogical reasoning abilities. Cereb Cortex. 26:915–932.

Amunts K, Lepage C, Borgeat L, Mohlberg H, Dickscheid T, Rousseau ME, Bludau S, Bazin PL, Lewis LB, Oros-Peusquens AM, et al. 2013. BigBrain: an ultrahigh-resolution 3D human brain model. Science. 340:1472–1475.

Anderson JLR, Jenkinson M, Smith S. 2007. Non-linear registration aka Spatial normalisation. FMRIB Technial Report TR07JA2.

Andersson JL, Skare S, Ashburner J. 2003. How to correct susceptibility distortions in spin-echo echo-planar images: application to diffusion tensor imaging. Neuroimage. 20:870–888.

Andersson JLR, Xu J, Yacoub E, Auerbach E, Moeller S, Ugurbil K editors. 2012. A comprehensive Gaussian process Framework for correcting distortions and movements in diffusion images. In. ISMRM, Melbourne, Australia.

Anwander A, Tittgemeyer M, von Cramon DY, Friederici AD, Knösche TR. 2007. Connectivity-based parcellation of Broca's area. Cereb Cortex. 17:816–825.

Aristotle. 350BC reprinted in 2004. On the Parts of Animals.

Avants BB, Duda JT, Zhang H, Gee JC. 2007. Multivariate normalization with symmetric diffeomorphisms for multivariate studies. Med Image Comput Comput Assist Interv. 10:359–366.

Avants BB, Epstein CL, Grossman M, Gee JC. 2008. Symmetric diffeomorphic image registration with cross-correlation: evaluating automated labeling of elderly and neurodegenerative brain. Med Image Anal. 12:26–41.

Azuar C, Reyes P, Slachevsky A, Volle E, Kinkingnehun S, Kouneiher F, Bravo E, Dubois B, Koechlin E, Levy R. 2014. Testing the model of caudo-rostral organization of cognitive control in the human with frontal lesions. Neuroimage. 84:1053–1060.

Badre D. 2008. Cognitive control, hierarchy, and the rostro-caudal organization of the frontal lobes. Trends Cogn Sci. 12:193–200.

Badre D, D'Esposito M. 2007. Functional magnetic resonance imaging evidence for a hierarchical organization of the prefrontal cortex. J Cogn Neurosci. 19:2082–2099.

Badre D, D'Esposito M. 2009. Is the rostro-caudal axis of the frontal lobe hierarchical? Nat Rev Neurosci. 10:659–669.

Badre D, Hoffman J, Cooney JW, D'Esposito M. 2009. Hierarchical cognitive control deficits following damage to the human frontal lobe. Nat Neurosci. 12:515–522.

Basser PJ, Pajevic S, Pierpaoli C, Duda J, Aldroubi A. 2000. In vivo fiber tractography using DT-MRI data. Magn Reson Med. 44:625–632.

Basser PJ, Pierpaoli C. 1996. Microstructural and physiological features of tissues elucidated by quantitative-diffusion-tensor MRI. J Magn Reson B. 111:209–219.

Behrens TE, Johansen-Berg H, Woolrich MW, Smith SM, Wheeler-Kingshott CA, Boulby PA, Barker GJ, Sillery EL, Sheehan K, Ciccarelli O, et al. 2003. Non-invasive mapping of connections between human thalamus and cortex using diffusion imaging. Nat Neurosci. 6:750–757.

Blits KC. 1999. Aristotle: form, function, and comparative anatomy. Anat Rec. 257:58–63.

Bludau S, Eickhoff SB, Mohlberg H, Caspers S, Laird AR, Fox PT, Schleicher A, Zilles K, Amunts K. 2014. Cytoarchitecture, probability maps and functions of the human frontal pole. Neuroimage. 93 Pt 2:260–275.

Broca P. 1863. Localisation des fonctions cérébrales. Siège du langage articulé. Bull Soci Anthropol. 4:200–208.

Burgess PW, Alderman N, Volle E, Benoit RG, Gilbert SJ. 2009. Mesulam's frontal lobe mystery re-examined. Restor Neurol Neurosci. 27:493–506.

Carmichael ST, Price JL. 1996. Connectional networks within the orbital and medial prefrontal cortex of macaque monkeys. J Comp Neurol. 371:179–207.

Caruyer E, Lenglet C, Sapiro G, Deriche R. 2013. Design of multishell sampling schemes with uniform coverage in diffusion MRI. Magn Reson Med. 69:1534–1540.

Caspers S, Eickhoff SB, Zilles K, Amunts K. 2013. Microstructural grey matter parcellation and its relevance for connectome analyses. Neuroimage. 80:18–26.

Catani M, Dell'Acqua F, Budisavljevic S, Howells H, Thiebaut de Schotten M, Froudist-Walsh S, D'Anna L, Thompson A, Sandrone S, Bullmore ET, et al. 2016. Frontal networks in adults with autism spectrum disorder. Brain. 139:616–630.

Cattell RB. 1966. The Scree Test For The Number Of Factors. Multivariate Behav Res. 1:245–276.

Christoff K, Keramatian K, Gordon AM, Smith R, Madler B. 2009. Prefrontal organization of cognitive control according to levels of abstraction. Brain Res. 1286:94–105.

Christoff K, Prabhakaran V, Dorfman J, Zhao Z, Kroger JK, Holyoak KJ, Gabrieli JD. 2001. Rostrolateral prefrontal cortex involvement in relational integration during reasoning. Neuroimage. 14:1136–1149.

Connor JR, Pinero DJ. 2005. Iron and brain function. In: Lieberman HR, Kanarek RB, Prasa C, editors. Nutritional Neuroscience. Boca Raton: CRC Press Taylor & Francis Group. p. 235–260

Conturo TE, Lori NF, Cull TS, Akbudak E, Snyder AZ, Shimony JS, McKinstry RC, Burton H, Raichle ME. 1999. Tracking neuronal fiber pathways in the living human brain. Proc Natl Acad Sci U S A. 96:10422–10427.

Conturo TE, McKinstry RC, Aronovitz JA, Neil JJ. 1995. Diffusion MRI: precision, accuracy and flow effects. NMR Biomed. 8:307–332.

Das SR, Avants BB, Grossman M, Gee JC. 2009. Registration based cortical thickness measurement. Neuroimage. 45: 867–879.

Deoni SC, Mercure E, Blasi A, Gasston D, Thomson A, Johnson M, Williams SC, Murphy DG. 2011. Mapping infant brain myelination with magnetic resonance imaging. J Neurosci. 31:784–791.

Domenech P, Koechlin E. 2015. Executive control and decision-making in the prefrontal cortex. Curr Opin Behav Sci. 1: 101–106.

Ecker C, Andrews D, Dell'Acqua F, Daly E, Murphy C, Catani M, Thiebaut de Schotten M, Baron-Cohen S, Lai MC, Lombardo MV, et al. 2016. Relationship between cortical gyrification, white matter connectivity, and autism spectrum disorder. Cereb Cortex. 26:3297–3309.

Ecker C, Bookheimer SY, Murphy DG. 2015. Neuroimaging in autism spectrum disorder: brain structure and function across the lifespan. Lancet Neurol. 14:1121–1134.

Feinberg DA, Moeller S, Smith SM, Auerbach E, Ramanna S, Gunther M, Glasser MF, Miller KL, Ugurbil K, Yacoub E. 2010. Multiplexed echo planar imaging for sub-second whole brain FMRI and fast diffusion imaging. PLoS One. 5:e15710.

Fellows L. 2012.Decision-making: executive functions meet motivation. In: Stuss D, Knight R, editors. Principles of frontal lobe function. NewYork: Oxford University Press. p. 490–500.

Flechsig PE. 1920.Anatomie des menschlichen Gehirns und Rückenmarks auf myelogenetischer Grundlage. Leipzig: Thieme.

Fonov V, Evans AC, Botteron K, Almli CR, McKinstry RC, Collins DL, Brain Development Cooperative G. 2011. Unbiased average age-appropriate atlases for pediatric studies. Neuroimage. 54:313–327.

Geschwind N, Galaburda AM. 1985. Cerebral lateralization. Biological mechanisms, associations, and pathology: I. A hypothesis and a program for research. Arch Neurol. 42:428–459.

Gilbert SJ, Gonen-Yaacovi G, Benoit RG, Volle E, Burgess PW. 2010. Distinct functional connectivity associated with lateral versus medial rostral prefrontal cortex: a meta-analysis. Neuroimage. 53:1359–1367.

Glasser MF, Van Essen DC. 2011. Mapping human cortical areas in vivo based on myelin content as revealed by T1- and T2-weighted MRI. J Neurosci. 31:11597–11616.

Gonen-Yaacovi G, de Souza LC, Levy R, Urbanski M, Josse G, Volle E. 2013. Rostral and caudal prefrontal contribution to creativity: a meta-analysis of functional imaging data. Front Hum Neurosci. 7:465.

Gorgolewski KJ, Varoquaux G, Rivera G, Schwartz Y, Sochat VV, Ghosh SS, Maumet C, Nichols TE, Poline JB, Yarkoni T, et al. 2016. NeuroVault.org: a repository for sharing unthresholded statistical maps, parcellations, and atlases of the human brain. Neuroimage. 124:1242–1244.

Gorgolewski KJ, Varoquaux G, Rivera G, Schwarz Y, Ghosh SS, Maumet C, Sochat VV, Nichols TE, Poldrack RA, Poline JB, et al. 2015. NeuroVault.org: a web-based repository for collecting and sharing unthresholded statistical maps of the human brain. Front Neuroinform. 9:8.

Griffanti L, Salimi-Khorshidi G, Beckmann CF, Auerbach EJ, Douaud G, Sexton CE, Zsoldos E, Ebmeier KP, Filippini N, Mackay CE, et al. 2014. ICA-based artefact removal and accelerated fMRI acquisition for improved resting state network imaging. Neuroimage. 95:232–247.

Hobeika L, Diard-Detoeuf C, Garcin B, Levy R, Volle E. 2016. General and specialized brain correlates for analogical reasoning: a meta-analysis of functional imaging studies. Hum Brain Mapp. 37:1953–1969.

Holmes CJ, Hoge R, Collins L, Woods R, Toga AW, Evans AC. 1998. Enhancement of MR images using registration for signal averaging. J Comput Assist Tomogr. 22:324–333.

Hopf A. 1956. Distribution of myeloarchitectonic marks in the frontal cerebral cortex in man. J Hirnforsch. 2:311–333.

Jacobs B, Schall M, Prather M, Kapler E, Driscoll L, Baca S, Jacobs J, Ford K, Wainwright M, Treml M. 2001. Regional dendritic and spine variation in human cerebral cortex: a quantitative golgi study. Cereb Cortex. 11:558–571.

Jbabdi S, Behrens TE. 2013. Long-range connectomics. Ann N Y Acad Sci. 1305:83–93.

Jenkinson M, Bannister P, Brady M, Smith S. 2002. Improved optimization for the robust and accurate linear registration and motion correction of brain images. Neuroimage. 17: 825–841.

Jennings RG, Van Horn JD. 2012. Publication bias in neuroimaging research: implications for meta-analyses. Neuroinformatics. 10:67–80.

Johansen-Berg H, Behrens TEJ, Robson MD, Drobnjak I, Rushworth MFS, Brady JM, Smith SM, Higham DJ, Matthews PM. 2004. Changes in connectivity profiles define functionally distinct regions in human medial frontal cortex. Proc Natl Acad Sci U S A. 101:13335–13340.

Jones DK. 2008. Studying connections in the living human brain with diffusion MRI. Cortex. 44:936–952.

Jones DK. 2010. Challenges and limitations of quatifying brain connectivity in vivo with diffusion MRI. Imaging Med. 2:341–355.

Jones DK, Griffin LD, Alexander DC, Catani M, Horsfield MA, Howard RJ, Williams SC. 2002. Spatial normalization and averaging of diffusion tensor MRI data sets. NeuroImage. 17:592–617.

Jones DK, Knosche TR, Turner R. 2013. White matter integrity, fiber count, and other fallacies: the do's and don'ts of diffusion MRI. Neuroimage. 73:239–254.

Karnath H-O, Himmelbach M, Rorden C. 2002. The subcortical anatomy of human spatial neglect: putamen, caudate nucleus and pulvinar. Brain. 125:350–360.

Karnath HO, Ferber S, Himmelbach M. 2001. Spatial awareness is a function of the temporal not the posterior parietal lobe. Nature. 411:950–953.

Klein A, Andersson J, Ardekani BA, Ashburner J, Avants B, Chiang MC, Christensen GE, Collins DL, Gee J, Hellier P, et al. 2009. Evaluation of 14 nonlinear deformation algorithms applied to human brain MRI registration. NeuroImage. 46:786–802.

Klein JC, Behrens TE, Robson MD, Mackay CE, Higham DJ, Johansen-Berg H. 2007. Connectivity-based parcellation of human cortex using diffusion MRI: establishing reproducibility, validity and observer independence in BA 44/45 and SMA/pre-SMA. Neuroimage. 34:204–211.

Koechlin E, Basso G, Pietrini P, Panzer S, Grafman J. 1999. The role of the anterior prefrontal cortex in human cognition. Nature. 399:148–151.

Koechlin E, Ody C, Kouneiher F. 2003. The architecture of cognitive control in the human prefrontal cortex. Science. 302:1181–1185.

Koechlin E, Summerfield C. 2007. An information theoretical approach to prefrontal executive function. Trends Cogn Sci. 11:229–235.

Kroger JK, Sabb FW, Fales CL, Bookheimer SY, Cohen MS, Holyoak KJ. 2002. Recruitment of anterior dorsolateral prefrontal cortex in human reasoning: a parametric study of relational complexity. Cereb Cortex. 12:477–485.

Le Ber I, Guedj E, Gabelle A, Verpillat P, Volteau M, Thomas-Anterion C, Decousus M, Hannequin D, Vera P, Lacomblez L, et al. 2006. Demographic, neurological and behavioural characteristics and brain perfusion SPECT in frontal variant of frontotemporal dementia. Brain. 129:3051–3065.

Li W, Qin W, Liu H, Fan L, Wang J, Jiang T, Yu C. 2013. Subregions of the human superior frontal gyrus and their connections. Neuroimage. 78:46–58.

Liu H, Qin W, Li W, Fan L, Wang J, Jiang T, Yu C. 2013. Connectivity-based parcellation of the human frontal pole with diffusion tensor imaging. J Neurosci. 33:6782–6790.

Mazoyer B, Zago L, Jobard G, Crivello F, Joliot M, Perchey G, Mellet E, Petit L, Tzourio-Mazoyer N. 2014. Gaussian mixture modeling of hemispheric lateralization for language in a large sample of healthy individuals balanced for handedness. PLoS One. 9:e101165.

Merker B. 1983. Silver staining of cell bodies by means of physical development. J Neurosci Methods. 9:235–241.

Mesulam M. 2000.Bahavioral neuroanatomy: large-scale networks, association cortex, frontal syndromes, the limbic system, and hemispheric specializations. In: Mesulam M, editor. Principles of behavioral and cognitive neurology, 2nd ed. Oxford University Press. p. 1–91.

Mesulam M. 2005. Imaging connectivity in the human cerebral cortex: the next frontier? Ann Neurol. 57:5–7.

Moeller S, Yacoub E, Olman CA, Auerbach E, Strupp J, Harel N, Ugurbil K. 2010. Multiband multislice GE-EPI at 7 tesla, with 16-fold acceleration using partial parallel imaging with application to high spatial and temporal whole-brain fMRI. Magn Reson Med. 63:1144–1153.

Moseley ME, Cohen Y, Kucharczyk J, Mintorovitch J, Asgari HS, Wendland MF, Tsuruda J, Norman D. 1990. Diffusion-weighted MR imaging of anisotropic water diffusion in cat central nervous system. Radiology. 176:439–445.

Ongur D, Price JL. 2000. The organization of networks within the orbital and medial prefrontal cortex of rats, monkeys and humans. Cereb Cortex. 10:206–219.

Passingham RE. 1973. Anatomical differences between the neocortex of man and other primates. Brain Behav Evol. 7:337–359.

Rojkova K, Volle E, Urbanski M, Humbert F, Dell'Acqua F, Thiebaut de Schotten M. 2016. Atlasing the frontal lobe connections and their variability due to age and education: a spherical deconvolution tractography study. Brain Struct Funct. 221:1751–1766.

Salimi-Khorshidi G, Douaud G, Beckmann CF, Glasser MF, Griffanti L, Smith SM. 2014. Automatic denoising of functional MRI data: combining independent component analysis and hierarchical fusion of classifiers. Neuroimage. 90:449–468.

Sallet J, Mars RB, Noonan MP, Neubert FX, Jbabdi S, O'Reilly JX, Filippini N, Thomas AG, Rushworth MF. 2013. The organization of dorsal frontal cortex in humans and macaques. J Neurosci. 33:12255–12274.

Saygin ZM, Osher DE, Koldewyn K, Reynolds G, Gabrieli JD, Saxe RR. 2012. Anatomical connectivity patterns predict face selectivity in the fusiform gyrus. Nat Neurosci. 15:321–327.

Schubotz RI, Anwander A, Knosche TR, von Cramon DY, Tittgemeyer M. 2010. Anatomical and functional parcellation of the human lateral premotor cortex. Neuroimage. 50:396–408.

Semendeferi K, Armstrong E, Schleicher A, Zilles K, Van Hoesen GW. 2001. Prefrontal cortex in humans and apes: a comparative study of area 10. Am J Phys Anthropol. 114:224–241.

Semendeferi K, Lu A, Schenker N, Damasio H. 2002. Humans and great apes share a large frontal cortex. Nat Neurosci. 5:272–276.

Setsompop K, Gagoski BA, Polimeni JR, Witzel T, Wedeen VJ, Wald LL. 2012. Blipped-controlled aliasing in parallel imaging for simultaneous multislice echo planar imaging with reduced g-factor penalty. Magn Reson Med. 67: 1210–1224.

Smith R, Keramatian K, Christoff K. 2007. Localizing the rostrolateral prefrontal cortex at the individual level. Neuroimage. 36:1387–1396.

Smith SM. 2002. Fast robust automated brain extraction. Hum Brain Mapp. 17:143–155.

Smith SM, Jenkinson M, Woolrich MW, Beckmann CF, Behrens TEJ, Johansen-Berg H, Bannister PR, De Luca M, Drobnjak I, Flitney DE, et al. 2004. Advances in functional and structural MR image analysis and implementation as FSL. NeuroImage. 23:208–219.

Smith SM, Jenkinson M, Woolrich MW, Beckmann CF, Behrens TEJ, Johansen-Berg H, Bannister PR, De Luca M, Drobnjak I, Flitney DE, et al. 2004. Advances in functional and structural MR image analysis and implementation as FSL. Neuroimage. 23 Suppl 1:S208–219.

Sokunbi MO, Staff RT, Waiter GD, Ahearn TS, Fox HC, Deary IJ, Starr JM, Whalley LJ, Murray AD. 2011. Inter-individual differences in fMRI entropy measurements in old age. IEEE Trans Biomed Eng. 58:3206–3214.

Sotiropoulos SN, Aganj I, Jbabdi S, Sapiro G, Lenglet C, Behrens TE. 2011. Inference on constant solid angle orientation distribution functions from diffusion-weighted MRI. In. OHBM. Quebec, Canada.

Sotiropoulos SN, Jbabdi S, Xu J, Andersson JL, Moeller S, Auerbach EJ, Glasser MF, Hernandez M, Sapiro G, Jenkinson M, et al. 2013. Advances in diffusion MRI acquisition and processing in the Human Connectome Project. Neuroimage. 80:125–143.

Thiebaut de Schotten M, Urbanski M, Duffau H, Volle E, Levy R, Dubois B, Bartolomeo P. 2005. Direct evidence for a parietal-frontal pathway subserving spatial awareness in humans. Science. 309:2226–2228.

Thiebaut de Schotten M, Urbanski M, Valabregue R, Bayle DJ, Volle E. 2014. Subdivision of the occipital lobes: an anatomical and functional MRI connectivity study. Cortex. 56:121–137.

Tomassini V, Jbabdi S, Klein JC, Behrens TE, Pozzilli C, Matthews PM, Rushworth MF, Johansen-Berg H. 2007. Diffusion-weighted imaging tractography-based parcellation of the human lateral premotor cortex identifies dorsal and ventral subregions with anatomical and functional specializations. J Neurosci. 27:10259–10269.

Travis K, Ford K, Jacobs B. 2005. Regional dendritic variation in neonatal human cortex: a quantitative Golgi study. Dev Neurosci. 27:277–287.

Tuch D, Wisco JJ, Khachaturian M, Ekstrom L, Ko¨tter R, Vanduffel W. 2005. Q-ball imaging of macaque white matter architecture. Philos Trans R Soc Lond B Biol Sci. 360:869–879.

Turner R, Le Bihan D, Maier J, Vavrek R, Hedges LK, Pekar J. 1990. Echo-planar imaging of intravoxel incoherent motion. Radiology. 177:407–414.

Tustison NJ, Avants BB. 2013. Explicit B-spline regularization in diffeomorphic image registration. Front Neuroinform. 7:39.

Tustison NJ, Cook PA, Klein A, Song G, Das SR, Duda JT, Kandel BM, van Strien N, Stone JR, Gee JC, et al. 2014. Large-scale evaluation of ANTs and FreeSurfer cortical thickness measurements. Neuroimage. 99:166–179.

Ugurbil K, Xu J, Auerbach EJ, Moeller S, Vu AT, Duarte-Carvajalino JM, Lenglet C, Wu X, Schmitter S, Van de Moortele PF, et al. 2013. Pushing spatial and temporal resolution for functional and diffusion MRI in the Human Connectome Project. Neuroimage. 80:80–104.

Urbanski M, Brechemier ML, Garcin B, Bendetowicz D, Thiebaut de Schotten M, Foulon C, Rosso C, Clarencon F, Dupont S, Pradat-Diehl P, et al. 2016. Reasoning by analogy requires the left frontal pole: lesion-deficit mapping and clinical implications. Brain. 139:1783–1799.

van den Heuvel MP, de Reus MA, Feldman Barrett L, Scholtens LH, Coopmans FM, Schmidt R, Preuss TM, Rilling JK, Li L.

2015. Comparison of diffusion tractography and tract-tracing measures of connectivity strength in rhesus macaque connectome. Hum Brain Mapp. 36:3064–3075.

Van Essen DC, Maunsell JHR. 1983. Hierarchical organization and functional streams in the visual cortex. Trends Neurosci. 6:370–375.

Van Essen DC, Smith SM, Barch DM, Behrens TE, Yacoub E, Ugurbil K, Consortium WU-MH. 2013. The WU-Minn Human Connectome Project: an overview. Neuroimage. 80:62–79.

Vartanian O. 2012. Dissociable neural systems for analogy and metaphor: implications for the neuroscience of creativity. Br J Psychol. 103:302–316.

Volle E, Gilbert SJ, Benoit RG, Burgess PW. 2010. Specialization of the rostral prefrontal cortex for distinct analogy processes. Cereb Cortex. 20:2647–2659.

Volle E, Gonen-Yaacovi G, Costello Ade L, Gilbert SJ, Burgess PW. 2011. The role of rostral prefrontal cortex in prospective memory: a voxel-based lesion study. Neuropsychologia. 49:2185–2198.

Wagstyl K, Ronan L, Goodyer IM, Fletcher PC. 2015. Cortical thickness gradients in structural hierarchies. Neuroimage. 111:241–250.

Watson RT, Valenstein E, Heilman KM. 1981. Thalamic neglect. Possible role of the medial thalamus and nucleus reticularis in behavior. Arch Neurol. 38:501–506.

Waxman SG, Bennett MV. 1972. Relative conduction velocities of small myelinated and non-myelinated fibres in the central nervous system. Nat New Biol. 238:217–219.

Xu J, Moeller S, Strupp J, Auerbach E, Feinberg D, Ugurbil K, Yacoub E. 2012. Highly accelerated whole brain imaging using aligned-blipped-controlled-aliasing multiband EPI. Proc Int Soc Mag Reson Med. 20:2306.

Yao Y, Lu WL, Xu B, Li CB, Lin CP, Waxman D, Feng JF. 2013. The increase of the functional entropy of the human brain with age. Sci Rep. 3:2853.

Yarkoni T, Poldrack RA, Nichols TE, Van Essen DC, Wager TD. 2011. Large-scale automated synthesis of human functional neuroimaging data. Nat Methods. 8:665–670.

Zhang Y, Brady M, Smith SM. 2001. Segmentation of brain MR images through a hidden Markov random field model and the expectation-maximization algorithm. IEEE Trans Med Imaging. 20:45–57.

Zilles K, Amunts K. 2015.Anatomical basis for functional specialization. In: Uludağ K, Uğurbil K, Berliner L, editors. fMRI: from nuclear spins to brain functions. New York: Springer. p. 27–66.